Nano Research
2019, 12(6): 1313–1320

ISSN 1998-0124 CN 11-5974/O4
https://doi.org/10.1007/s12274-018-2262-y

Research Article

Shape-controlled synthesis of liquid metal nanodroplets for photothermal therapy

Junjie Yan[1,2,3,4,§], Xudong Zhang[1,3,4,§], Yang Liu[5], Yanqi Ye[1,3,4], Jicheng Yu[1,3,4], Qian Chen[1,3,4], Jinqiang Wang[1,3,4], Yuqi Zhang[1,3,4], Quanyin Hu[1,3,4], Yang Kang[1,3,4], Min Yang[2] (✉), and Zhen Gu[1,3,4,6,7] (✉)

[1] *Joint Department of Biomedical Engineering, University of North Carolina at Chapel Hill and North Carolina State University, Raleigh, NC 27695, USA*
[2] *Molecular Imaging Center, Key Laboratory of Nuclear Medicine, Ministry of Health, Jiangsu Key Laboratory of Molecular Nuclear Medicine, Jiangsu Institute of Nuclear Medicine, Wuxi 214063, China*
[3] *Department of Bioengineering, University of California, Los Angeles, CA 90095, USA*
[4] *California NanoSystems Institute, University of California, Los Angeles, CA 90095, USA*
[5] *Department of Materials Science & Engineering, North Carolina State University, Raleigh, NC 27695, USA*
[6] *Jonsson Comprehensive Cancer Center, University of California, Los Angeles, CA 90095, USA*
[7] *Center for Minimally Invasive Therapeutics, University of California, Los Angeles, CA 90095, USA*
[§] *Junjie Yan and Xudong Zhang contributed equally to this work.*

Received: 10 October 2018 / **Revised:** 30 November 2018 / **Accepted:** 3 December 2018

ABSTRACT

The capping agents for liquid metal (LM) nanodroplets in aqueous solutions are restricted to thiol-containing and positively-charged molecules or macromolecules. However, both thiolate-metal complex and electrostatic interaction are liable to detachment upon strong mechanical forces such as sonication, leading to limited stability and applications. To address this, we utilized ultrasmall water soluble melanin nanoparticles (MNPs) as the capping agent, which exhibited strong metal binding capability with the oxide layer of gallium based LMs and resulted in enhanced stability. Interestingly, shape-controlled synthesis of LM nanodroplets can be achieved by the incorporation of MNPs. Various EGaIn nanostructures including nanorice, nanosphere and nanorod were obtained by simply tuning the feed ratio, sonication time, and suspension temperature. Among these shapes, EGaIn nanorice has the best photothermal conversion efficiency, which could be leveraged for photothermal therapy.

KEYWORDS

liquid metal, melanin nanoparticles, nanomedicine, shape-controlled synthesis, photothermal therapy

1 Introduction

Metal or alloy nanoparticles with specific shapes are of interest in multiple applications including catalysis, imaging, sensing, data storage and biomedicine [1–6]. Current and primary strategies towards shape-controlled synthesis of metal or alloy nanoparticles basically consist of bottom-up and top-down approaches, through which particulates with a variety of shapes, sizes, and size distributions can be achieved [7]. Bottom-up approach typically involves the (bio)chemical reduction of metal salts, while the top-down method mainly processes a macroscopic metal into the desired size scale in physical manners (grilling, grinding, microfluidics, stretching, photolithography, imprint lithography, particle replication in non-wetting templates (PRINT), etc.) [8–11]. However, it remains challenging to control the shapes of nanoparticles from soft metals or alloys, especially liquid metals (LMs), whose melting points are near or below the room temperature. In the past decade, gallium based LMs (commercial sources include Ga, eutectic gallium indium (EGaIn), and eutectic gallium indium tin (Galinstan) have emerged as notable inorganic candidates in various fields, ranging from energy, catalysis, electronics to biomedical applications, primarily attributing to their superior fluidity and low toxicity compared to conventional metals [12–17]. Additionally, the sonication strategy with the utilization of surfactants has facilitated facile synthesis of LMs in the nanoscale with good solubility and stability in aqueous solutions, significantly extending their performances in biomedical theranostics [18–21].

Generally, large surface tension renders LMs with a spherical shape to minimize surface energy, yet both laser irradiation and heating could induce the transformation of LM nanodroplets and exhibit a capping agent (or a surfactant) dependent profile [22, 23]. Thiol-containing molecules are a primary category of capping agents for LM nanodroplets, which is based on the formation of a metal thiolate complex [24]. However, thiol groups are liable to coupling in oxidative conditions, such as a reactive oxygen species (ROS) microenvironment [25], whose formation has been confirmed in the process of sonication [22, 26]. Recently, Lin et al. demonstrated that positively-charged surfactants could also stabilize the suspension via the electrostatic interactions with the negatively-charged oxide layer of LM nanodroplets [23]. Aside from these two kinds of interactions, melanin or polydopamine can provide coordination or chelating interaction towards various materials, including metal ions and metal oxides [27, 28]. Moreover, processing melanins into ultrasmall nanoscale (< 10 nm) can significantly enhance their metal chelating capacity [29].

Photothermal therapy (PTT) has been leveraged as a promising

Address correspondence to Zhen Gu, guzhen@ucla.edu; Min Yang, yangmin@jsinm.org

ablation approach for the treatment of various disease with the employment of photothermal agents, which can absorb light and enhance the tissue heating upon light irradiation. So far, various photothermal agents have been developed, mainly including original gold nanorods [30], gold nanoshells [31], organic nanoparticles [32], porphysomes [33], and naphthalocyanine micelles [34]. LMs have intrinsic thermal conductivity, but their significance in PTT has been seldomly studied. Herein, we leverage the ultrasmall water-soluble melanin nanoparticles (MNPs) as a capping agent for LM nanodroplets due to their excellent metal chelating ability and the unavoidable gallium oxide layer on the LM surface. Interestingly, by simply changing reaction parameters, such as the category of LMs, the concentration of MNPs, sonication period and temperature, LMs could be efficiently stabilized and generate various shapes including nanorice, nanosphere, and nanorod (Fig. 1(a)). This straightforward approach avoids the utilizations of complex additives, such as emulsifier, activator, and buffer, or harsh preparation procedure. The stability of these nanodroplets could be longer than two months. More significantly, among different shapes, LM nanorice presented the best photothermal efficiency (36.7%), which was higher than those of often reported gold nanorods [35], and thus performed as an excellent photothermal candidate for cancer ablation.

2 Results and discussions

Ultrasmall water-soluble MNPs were synthesized as our previous work [36, 37], with an average size of 3.1 ± 0.6 nm (Fig. S1 in the Electronic Supplementary Material (ESM)). Then, the aqueous mixture (12 mL) of EGaIn (80 μL) and MNPs (3 mg) were sonicated under an ice bath for a determined period. Interestingly, this formulation produced uniform EGaIn nanodroplets with a nanorice shape after 15 min sonication. This unique nanostructure has been reported in several materials by diverse methods, such as the self-assembly of block copolymers, and hydrothermal synthesis of metal (gold, silver, iron) nanoparticles and carbon dots [38–43]. However, LMs with such unique shape has only been obtained in the case of Galinstan via galvanic replacement [44].

As shown in Fig. 1(b), EGaIn nanorices have an aspect ratio (AR) of ~ 2.3 according to the transmission electron microscope (TEM). High resolution TEM and dark field scanning transmission electron microscopy (STEM) images show that EGaIn nanorices were, in fact, composed of small nanoparticles (Figs. 1(c) and 1(d)) [44]. Scanning electron microscope (SEM) and cryo-SEM images demonstrate the three-dimensional (3D) structure of the nanorice shape in both dry and liquid states (Figs. 1(e) and 1(f)). The structure and element analysis for the composition of EGaIn nanorices were explored by STEM-energy dispersive X-ray spectroscopy (STEM-EDS) elemental mapping and X-ray diffraction (XRD) patterns. Although the temperature of the mixture could slowly increase up to 60 °C within 20 min sonication, no obvious dealloying of indium (In) from EGaIn was observed (Figs. 1(g)–1(k)), which possibly resulted from insufficient temperature and heating period (typically 10 min around 70 °C) [23]. Aside from the pristine Ga and In elements, oxygen was evenly distributed through the EGaIn nanorices, and XRD

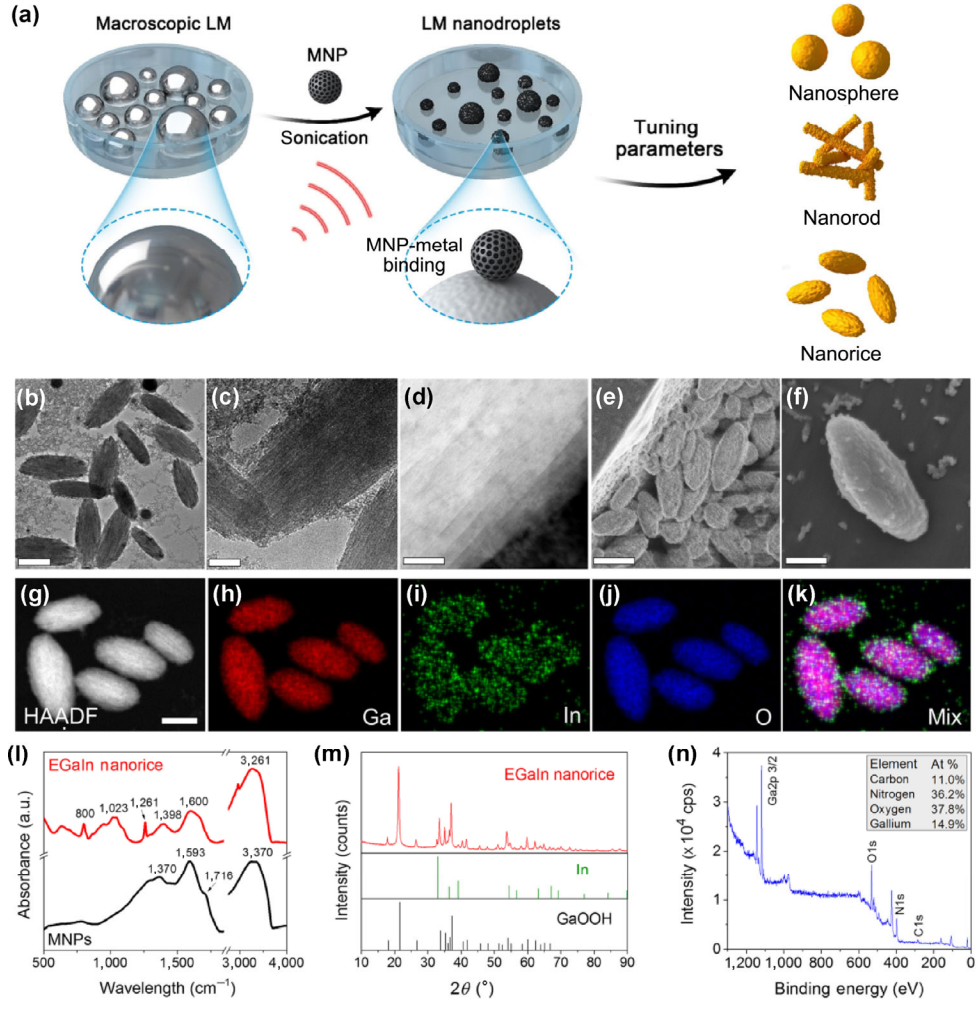

Figure 1 (a) Schematic of LM nanodroplets synthesis. (b)–(n) Characterizations of EGaIn nanorices. (b) TEM image, scale bar, 200 nm. (c) HRTEM image, scale bar, 50 nm. (d) Dark field STEM image of single EGaIn nanorice, scale bar, 50 nm. (e) SEM image, scale bar, 500 nm. (f) Cryo-SEM image, scale bar, 250 nm. (g)–(k) STEM image and EDS mapping, scale bar, 200 nm. (l) FTIR spectra. (m) XRD spectra. (n) XPS survey spectrum.

results verified their compositions of gallium oxide monohydroxide (GaO(OH)) and In (Fig. 1(m)), which was consistent with previous reports [22, 23].

To figure out the details of interactions between MNPs and EGaIn nanodroplets, Fourier-transform infrared (FTIR) spectra were measured. The FTIR spectrum of MNPs consists of several main bands centered at 1,370, 1,593, 1,716 and 3,370 cm^{-1} (Fig. 1(l)) [45]. The absorbance at 1,370 cm^{-1} attributes to the bending modes of OH, NH, and various kinds of aromatic rings. The bands at 1,593 and 3,370 cm^{-1} are due to the stretching modes of C=C and the OH bonds, respectively [46]. The signal at 1,716 cm^{-1} is assigned to C=O, revealing the presence of quinone group [47]. After interacting with EGaIn nanodroplets, the absorbance at 1,716 cm^{-1} decreased significantly. Meanwhile, two new absorbance at 1,023 and 1,261 cm^{-1} appeared, which are the bending band of Ga–OH [48] and stretching band of C–OH from carboxyl or phenolic OH [49], respectively. These data indicate that a quinone intermediate probably switched to a catechol and coordinated with the gallium oxide on the surface of EGaIn. To prove our hypothesis, X-ray photoelectron spectroscopy (XPS) was further used to evaluate the surface property of EGaIn nanorice and provide additional information for the binding interactions between MNPs and EGaIn nanodroplets. In Fig. 1(n), the survey spectrum indicates that the surface of EGaIn nanorices mainly contain carbon, oxygen, nitrogen and gallium elements. The high resolution C 1s spectrum reveals four different types of carbon: CH_x, C–NH_2; C–O, C–N; C=O and $\pi \rightarrow \pi^*$ species (Fig. S2 and Table S1 in the ESM) [45, 47]. From high resolution O 1s spectrum, it shows a predominant band at 531.6 eV corresponding to the formation of O–Ga, and the peak assigning to O–C at 530.3 eV is much stronger than that of O=C at 534.5 eV. Additionally, the high resolution Ga 3d spectrum demonstrates the presence of both Ga element and Ga^{3+}. The overall XPS data confirm that MNPs were successfully anchored onto the surface of EGaIn nanodroplets through multidentate chelating bonding between the catechol groups and the gallium oxide [28, 50]. The binding interactions between LM nanodroplets and MNPs were so strong that no color of MNPs was observed in the supernatant when gravity-induced precipitation of LM nanodroplets occurred (Fig. S3 in the ESM). Compared to thiol-containing and positively-charged molecules, MNPs presented better stability for EGaIn nanodroplets in aqueous solution (Fig. S4 in the ESM).

To probe the possible formation mechanism of EGaIn nanorice, we considered several factors on influencing the shapes of LM nanodroplets. First, we monitored the sonication mixture dynamically. UV–vis spectra represent that the absorbance at ~ 400 nm increased slowly as extending the sonication periods (Fig. 2(a)), and the color of the suspension gradually changed from dark grey to light grey. During the dynamic process, the corresponding sizes of EGaIn nanospheres did not show obvious change within 10 min by dynamic light scattering (DLS) and TEM (Figs. 2(b) and 2(d)), which possibly ascribed to the increased transmittance of the mixtures containing EGaIn nanodroplets. After 10 min, EGaIn nanospheres began to deform and merge, and subsequently formed nanorices with a polydispersity index (PDI) of 0.083 at 15 min. Prolonging sonication to 20 min increased the mixture temperature and led to slight aggregations of nanorices. However, further extending sonication periods to 30 and 40 min increased the mixture temperature more, but the sizes of EGaIn nanorices did not change significantly, and the shape of EGaIn nanorices was well retained (Fig. S5 in the ESM). Additionally, the zeta potential of EGaIn nanodroplets decreased throughout the sonication (Fig. 2(c)), suggesting that functional groups of MNPs including hydroxyl and carboxyl groups possibly participated in the capping process of EGaIn nanodroplets in addition to the catechol group.

Next, different concentrations of MNPs were explored to stabilize EGaIn nanodroplets. As shown in Fig. 3(a), the mass below 3 mg (0.25 $mg \cdot mL^{-1}$) could not produce stable EGaIn nanodroplets, which precipitated quickly within 10 min after fresh preparation. 3 mg feed of MNPs generated EGaIn nanorices, while a higher mass (> 3 mg) of MNPs produced EGaIn nanospheres (Fig. 3(d)). Notably, more addition of MNPs decreased the sizes of EGaIn nanospheres obviously, accompanying with more negative surface potentials (Figs. 3(b) and 3(c)). This could be explained that more MNPs provide more binding sites for EGaIn nanodroplets and thus decrease the possibility of their merging (or aggregation). However, other polymers such as hyaluronic acid (HA) with different concentrations did not present an obvious effect on the morphology of EGaIn nanodroplets (Fig. S6 in the ESM). Moreover, upon sonicating at room temperature or decreasing the volume (around 2/3) of the mixture, nanorod shape was achieved (Fig. S7 in the ESM).

Then, various polymers with different surface groups and charges were explored as capping agents for EGaIn nanodroplets (Figs. S8–S11 in the ESM). All formulations (3 mg polymers, 80 μL EGaIn in 12 mL DI water) were sonicated under an ice bath for 20 min. Briefly, positively-charged polyethylenimine (PEI) has good stabilizing ability and can disperse EGaIn into uniform nanospheres,

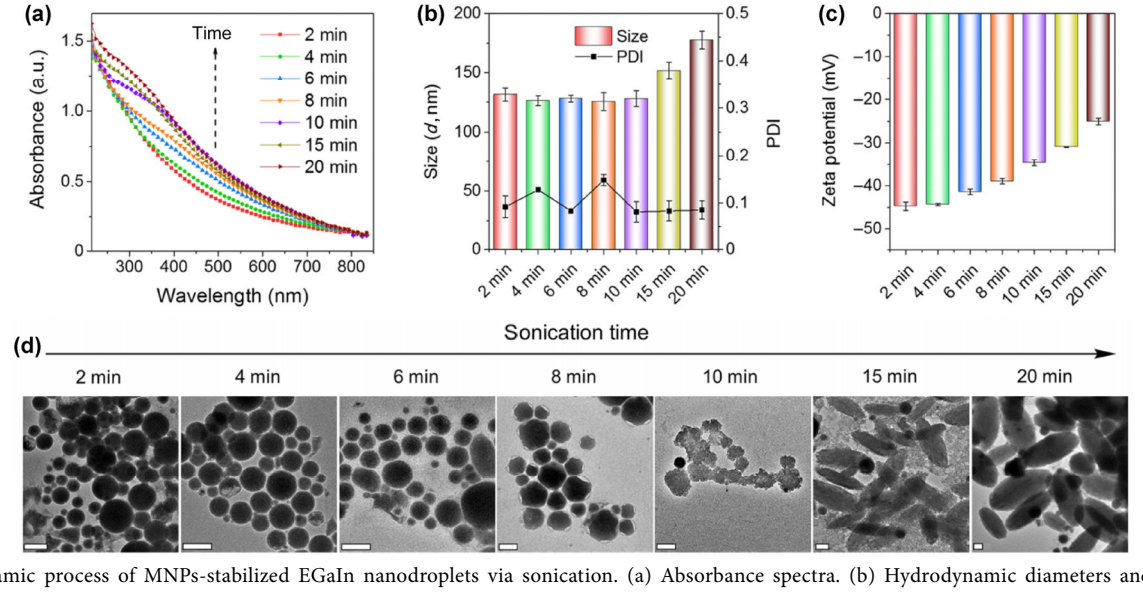

Figure 2 Dynamic process of MNPs-stabilized EGaIn nanodroplets via sonication. (a) Absorbance spectra. (b) Hydrodynamic diameters and PDI. (c) Zeta potentials. (d) TEM images with different sonication periods. Scale bar, 100 nm.

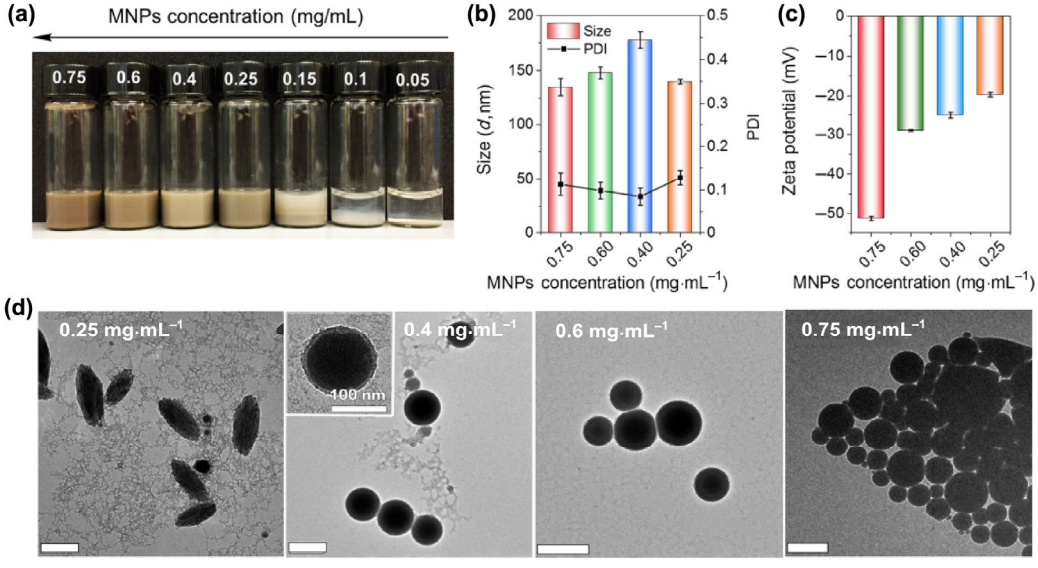

Figure 3 Concentration dependent profile of MNPs capped EGaIn nanodroplets. (a) Daylight images of EGaIn nanodroplet aqueous suspensions. (b) Hydrodynamic sizes and PDI. (c) Surface potentials. (d) TEM images, scale bar, 250 nm.

which is basically via the electrostatic interaction. Interestingly, HA could also stabilize EGaIn nanospheres via hydroxyl groups, but was with a relatively wide PDI. In the case of poly[2-(methacryloyloxy)ethyl]dimethyl-(3-sulfopropyl)ammonium hydroxide (PDMAPS), a neutral polymer, only random-shaped EGaIn nanodroplets could be produced. Collectively, polymers with reactive groups, including amino, thiol, and hydroxyl groups all can stabilize EGaIn nanodroplets, but their stabilizing efficacy and roles in controlling the shapes of LM nanodroplets differentiate significantly. Also, the influence of different LMs such as Galinstan and GaSn on the morphologies of final nanodroplets was investigated, utilizing MNPs as the capping agent. It was found that throughout the complete sonication periods (0–20 min), nanosphere was the only shape that was observed in both systems (Figs. S12 and S13 in the ESM).

Based on these observations, we postulate a plausible formation mechanism of EGaIn nanorices as follows. At the beginning, sonication efficiently processed macroscopic EGaIn into small nanoparticles by strong shear force. Simultaneously, MNPs multidentately chelated to the surface of gallium oxide via catechol groups, significantly improving the solubility and stability of EGaIn nanodroplets in aqueous solution. Then, heat and ROS generation from sonication gradually induced the generation of GaO(OH) [22]. As previously reported, GaO(OH) with a nanorice morphology (spindle-like, ellipsoid-like) could be synthesized via laser ablation of Ga metal, followed with an aging process (~ 7 days) in the presence of cetyltrimethylammonium bromide (CTAB) as a surfactant [51]. In our case, sonication produced gallium-containing clusters in addition to EGaIn nanospheres, with the stabilization by MNPs. Subsequently, continuous sonication and increased solution temperature facilitated the further growth of gallium clusters and resulted in the formation of EGaIn nanorice.

The same as conventional metals, LMs have excellent thermal conductivity and were once trialed as one kind of tumor ablation materials [52]. Chechetka et al. showed that LMs also had photothermal transduction capability upon near infrared (NIR) laser irradiation, despite its absorbance in the infrared region was not obvious as those of plasmonic materials or NIR dyes [19]. Processing LMs to nanodroplets with various shapes may potentially alter their photothermal properties, as in the case of gold nanoparticles [53]. Generally, the absorbance spectrum of LMs in the NIR region appears as a flat slope without typical absorbance peak, which is frequently observed in the circumstance of melanins and black phosphorus and good photothermal efficiency can still be achieved [54–56]. As shown in Fig. 4(a), the absorbance of EGaIn nanorods and nanorices were higher than that of EGaIn nanospheres, which possibly resulted from their larger sizes. Upon an 808 nm laser irradiation (2.0 W·cm^{-2}), the temperature of EGaIn nanorices suspension (0.5 mg·mL^{-1}) increased by 32.2 °C within 10 min, while the temperature increase of EGaIn nanorods and nanospheres suspensions were 28.8 and 23.7 °C respectively (Fig. 4(b)). In contrast, water exhibited only slight temperature increase (< 2 °C) under the same experimental conditions. Such photothermal heating effect was dependent on the concentration of EGaIn nanorices suspension and laser power (Figs. 4(c) and 4(d)). To further study the photostability of EGaIn nanorices, we also monitored the temperature variations for four heating-cooling cycles, no significant change of temperature elevation was found and the EGaIn nanorice suspension was still highly dispersed without precipitation (Fig. 4(e)). Such photostability was superior to many gold nanomaterials, whose nanostructures would often melt and lose typical absorbance upon repeated NIR laser irradiation [30, 57]. Additionally, according to Roper's method, the photothermal conversion efficiencies (η) of EGaIn nanodroplets suspensions were also calculated (see the ESM), and η for nanorice, nanorod and nanosphere were 36.7%, 28.8%, and 33.3% respectively (Fig. 4(f)). It should be noted that such high photothermal conversion efficiencies result from the intrinsic photothermal properties of LMs, but not from the MNPs, since capping with PEI could accomplish comparable photothermal effect (Fig. S14 in the ESM).

The excellent photothermal efficiency renders EGaIn nanorices a promising candidate for PTT [58]. To this end, we first tested the cytotoxicity of EGaIn nanorices (samples with 15 min sonication) against cancer cells by the cell counting kit-8 (CCK-8) assay. In Fig. 5(a), EGaIn nanorices presented negligible cytotoxicity towards 4T1 cells in the absence of laser even when the concentration was high up to 500 μg·mL^{-1}. In contrast, this concentration of EGaIn nanorices killed more than 90% of 4T1 cells upon continuous 808 nm NIR laser irradiation (1.6 W·cm^{-2}, 5 min), and this photothermal-induced cytotoxicity follows a concentration dependent manner. The *in vitro* cytotoxicity of EGaIn nanorices was also verified by Calcein AM/PI staining. Figure 5(b) reveals that cells treated with both EGaIn nanorices and laser irradiation suffer a significant cell death, while majority of 4T1 cells remain alive with treatment of EGaIn nanorices or laser irradiation separately. During

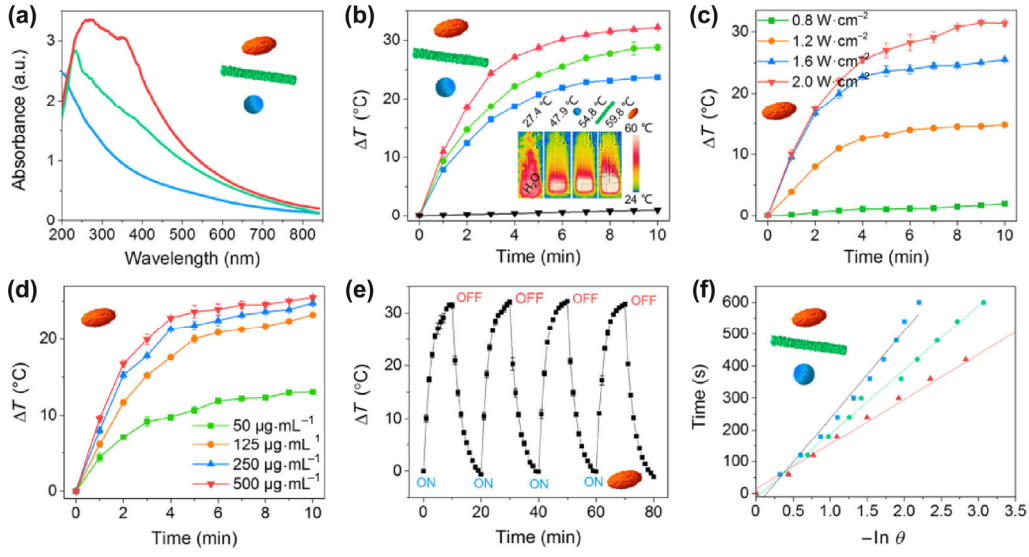

Figure 4 (a) Absorbance of EGaIn nanodroplets with different shapes. (b) Photothermal responses of EGaIn nanodroplets with different shapes upon NIR laser irradiation (808 nm, 2.0 W·cm^{-2}, 10 min). DI water was used to as control. Photothermal responses of melanin-stabilized EGaIn nanodroplets with various (c) power intensities and (d) concentrations and (e) four circles upon NIR laser irradiation (808 nm, 2.0 W·cm^{-2}, 500 μg·mL^{-1}). (f) Linearity curves fitted from the temperature cooling time vs. $-\ln(\Delta T/\Delta T_{max})$ of EGaIn nanodroplets with different shapes. The EGaIn nanodroplets concentration was 250 μg·mL^{-1}.

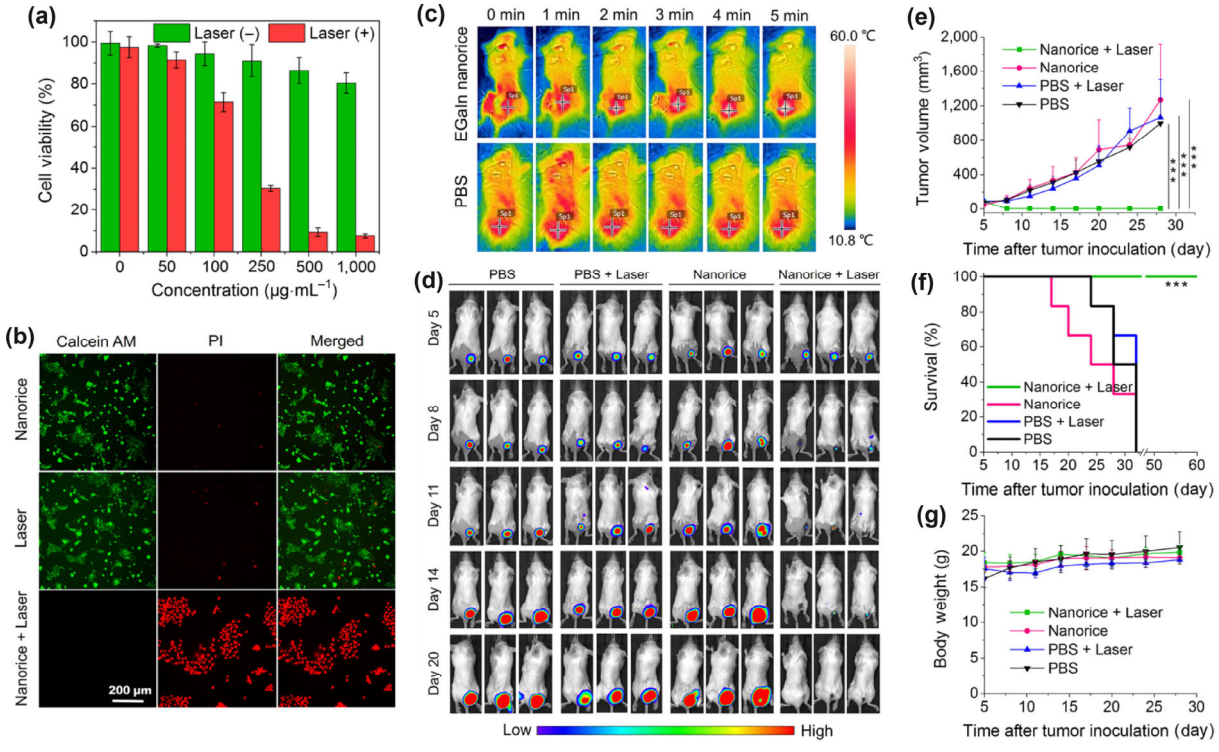

Figure 5 (a) Cytotoxicity of EGaIn nanorice with or without laser irradiation. (b) Calcein AM/PI staining of 4T1 cells with treatment using different formulations. (c) Thermal images of mice under laser irradiation (1.6 W·cm^{-2}, 5 min) at different time intervals. (d) *In vivo* bioluminescence imaging of the 4T1 tumor growth in mice treated (intratumoral injection, and the therapy started from the 5th day after tumor inoculation) with: PBS, PBS + Laser, EGaIn nanorice, and EGaIn nanorice + Laser (n = 6). (e) Average tumor volumes of treated mice (n = 6). Data are shown as the mean ± s.d. *** P < 0.001, two-way ANOVA with Tukey post-hoc test analyses. (f) Survival curves of mice receiving different treatments (n = 6). ***P < 0.001, by Log-Rank (Mantel-Cox) test. (g) Body weight curves of treated mice (n = 6). Data are shown as the mean ± s.d.

the continuous laser irradiation (5 min), the morphology of EGaIn nanorices was well retained without obvious shape transformation (Fig. S15 in the ESM).

To further evaluate the *in vivo* photothermal efficacy of EGaIn nanorices, 4T1 breast tumor model was established in the female Balb/c mice. To achieve a high utilization of photothermal agents and retain the shape EGaIn nanorices, we used intratumoral injection rather than intravenous injection. Twenty-four mice were randomly divided into four groups: untreated mice, mice with only EGaIn nanorices intratumoral injection (0.25 mg·kg^{-1}), mice with only laser irradiation, and mice with EGaIn nanorices injection and subsequent laser irradiation. Then, the mice were anaesthetized and the tumor was exposed to an 808 nm laser irradiation (1.6 W·cm^{-2}, 5 min). The real-time infrared thermal images of mice and the temperature variations in the tumor region during PTT were recorded every minute (Fig. 5(c)). For mice injected with EGaIn nanorices, the temperature of irradiated area increased remarkably from 32.4 to ~ 46.9 °C within 2 min and continuously increased to ~ 50.3 °C at

5 min, and this temperature is high enough for effective tumor ablation [59]. In contrast, the control group with only laser irradiation obtained a slight temperature increase (~ 2.5 °C) under the same condition, suggesting that EGaIn nanorices can convert light energy to heat effectively, and the conditions of the laser irradiation employed here would not result in hyperthermia and cause no damage to normal tissues. After the PTT, tumors that were treated with both EGaIn nanorices and laser irradiation generated dark burned scars, leaving a negligible amount of bioluminescence at the third day post treatment (Fig. 5(d)). During the following 60 days, no tumor recurrence was observed. In contrast, for groups treated with only EGaIn nanorices injection or laser irradiation, corresponding tumor volumes increased rapidly and exhibited a similar trend to those of untreated mice, and all these mice died within 27 days post treatment (Figs. 5(e) and 5(f)). These results accompanied with the hematoxylin and eosin (H&E) section (Fig. S16 in the ESM) suggested that EGaIn nanorices as a PPT agent could efficiently ablate the tumors. Moreover, PTT did not lead to significant body weight loss, indicating good biocompatibility of EGaIn nanorices (Fig. 5(g)).

3 Conclusions

In summary, ultrasmall MNPs can be exploited as a capping agent for the shape-controlled synthesis of LMs nanodroplets. By simply tuning the parameters such as the concentration of MNPs, sonication period and temperature, LMs nanodroplets can be readily dispersed in aqueous solutions and spontaneously self-assembled into various nanostructures including nanorice, nanosphere and nanorod. Of note, the unique EGaIn nanorices exhibit the best photothermal conversion efficiency in comparison to the nanosphere and nanorod. Accompanied with excellent photostability and biocompatibility, EGaIn nanorices can be harnessed as a promising PTT candidate for tumor ablation.

4 Methods

4.1 Synthesis of water-soluble melanin nanoparticles (MNPs)

Based on a previous method [29], melanin (50 mg) was dissolved in 20 mL of 0.1 N NaOH aqueous solution, followed by HCl aqueous solution (0.1 N) addition until the pH was neutral. The solution was then purified using Amicon® ultra centrifugal filters (MWCO = 30 kDa) and washed with deionized water to eliminate the salt. Freeze-drying gave the final black MNP powders with a yield of 65.4%.

4.2 Dynamic process of MNPs stabilized EGaIn/Galinstan/GaSn nanodroplets

MNPs (3.0 mg) and EGaIn (80 μL) were added into 12 mL deionized water and purged with argon for 10 min. During the sonication in an ice bath, every 2 mL aliquots of mixtures were dynamically (2, 4, 6, 10, 15, 20, 30, and 40 min) taken out. After sonication, the precipitated particles were discarded, and the remaining suspension was further subject to mild centrifugation (1,000 rpm) to remove large particles, and the resultant solution was kept as a stock solution for further use and characterizations. Dynamic MNPs stabilized Galinstan and GaSn nanodroplets were synthesized using the similar method.

4.3 Synthesis of methacrylated hyaluronic acid (m-HA)

m-HA was synthesized according to our previous work [60]. Typically, HA (2.0 g) was dissolved in 60 mL of deionized water at 4 °C, then methacrylic anhydride (MA, 1.6 mL) was slowly added into the solution. Through the reaction, the pH of the mixture was adjusted to 8–9 by the addition of 1 N NaOH and stirred at 4 °C for 30 h. Afterwards, the mixture was dialyzed against deionized water for 3 days. m-HA was achieved by lyophilization with a yield of 84.7%.

4.4 Synthesis of PDMAPS

PDMAPS was prepared using 4-cyano-4-(phenylcarbonothioylthio)pentanoic acid as a RAFT agent and ACVA as an initiator in a Schlenk tube, respectively. A representative example is as follows [61]: DMAPS (279.4 mg, 1.0 mmol), PEG950 (850 mg, 0.895 mmol), 4-cyano-4-(phenylcarbonothioylthio)pentanoic acid (18.6 mg, 0.067 mmol), ACVA (4.7 mg, 0.0168 mmol) were dissolved in 0.5 M sodium chloride solution with tuning pH to 7. Then, the solution was degassed by three freeze-evacuate-thaw cycles. The mixture was left at 70 °C preheated oil for 20 h. Later, the raw product was purified by dialysis against deionized water for 2 days and freeze-drying to give slight pink spongy powders. Yield: 87.6%.

4.5 Preparation of polymer stabilized LM (EGaIn and Galinstan) nanoparticles

Various polymers were employed as stabilizing reagents for the aqueous synthesis of liquid metal nanoparticles, including cationic, ionic and neutral polymers. In a typical procedure, 5 mg polymers (MNPs, PEI, HA and PDMAPS) were dissolved in 12 mL deionized water in a 50 mL filtration tube and purged with argon for 10 min. Then, the tube was subjected into the ice bath and added 80 μL LM (EGaIn and Galinstan). A Fisherbrand™ Model 505 Sonic dismembrator (Thermal Scientific) was used for sonication (frequency: 20 kHz; power rating: 500 Watts; probe diameter is 3 mm). The amplitude of the dismembrator was adjusted to 35% and the sonication proceeded for demanded time. After sonication, the precipitated particles were discarded, and the remaining suspension was further subject to mild centrifugation (1,000 rpm) to remove large particles, and the resultant solution was kept as a stock solution for further use.

4.6 *In vitro* photothermal cytotoxicity of EGaIn nanoparticles

4T1 cells were seeded in a 96-well plate at a density of 10^4 cells/well and incubated for 24 h. Then, the cells were incubated with EGaIn nanorice solutions at different concentrations (0, 50, 100, 250, 500, 1,000 μg·mL^{-1}, 100 μL/well) for 4 h. After PBS washing, all groups were replaced with fresh RPMI 1640 (50 μL), and then irradiated with an 808 nm laser for 5 min at a power intensity of 1.6 W·cm^{-2}. Similar procedure was performed in control groups while no laser irradiation was applied. Cell viability was examined following the standard procedure of CCK-8 assay.

4.7 *In vivo* photothermal ablation of tumors

All animals were treated in accordance with the Guide for Care and Use of Laboratory Animals, and was approved by the Institutional Animal Care and Use Committee (IACUC) of North Carolina State University. The tumor xenograft model was established on the female BALB/c mice (6 weeks, The Jackson Laboratory), with subcutaneous inoculation in the back with 1×10^6 4T1 cells. Five days after tumor inoculation, tumor volumes were around ~ 90 mm^3. The mice were divided into four groups (G1: EGaIn nanorice + Laser; G2: EGaIn nanorice; G3: PBS + Laser; G4: PBS) (n = 6). Mice were intratumorally injected with EGaIn nanorice, and the therapy started from the fifth day after tumor inoculation. In a typical photothermal therapy procedure, 25 μg EGaIn nanorice in 50 μL PBS were intratumorally injected into the tumor of the mice. Afterwards, laser irradiation (1.6 W·cm^{-2}) was employed for continuous irradiation on the tumor of mice for 5 min. The tumor burden was monitored via tumor bioluminescence and the images were captured on an IVIS Lumina imaging system (Perkin Elmer).

Acknowledgements

This work was supported by the grants from the Alfred P. Sloan Foundation (Sloan Research Fellowship), the National Natural Science Foundation of China (Nos. 21504034, 31671035, and 51473071), the National Key Research and Development Program of China (No. 2017ZX09304021), the Jiangsu Provincial Medical Innovation Team (No. CXTDA2017024), and Natural Science Foundation of Jiangsu Province (Nos. BK20161137, BK20170204, and BE2016632). This work was performed in part at the Analytical Instrumentation Facility (AIF) at North Carolina State University, which is supported by the State of North Carolina and the National Science Foundation (award number ECCS-1542015). The AIF is a member of the North Carolina Research Triangle Nanotechnology Network (RTNN), a site in the National Nanotechnology Coordinated Infrastructure (NNCI).

Electronic Supplementary Material: Supplementary material (materials, methods, further details of ligands synthesis, the photostability and cytotoxicity of LM nanodroplets, ^{1}H NMR spectra, TEM, cryo-SEM and EDS mapping measurements) is available in the online version of this article at https://doi.org/10.1007/s12274-018-2262-y.

References

[1] Sun, Y. G.; Xia, Y. N. Shape-controlled synthesis of gold and silver nanoparticles. *Science* **2002**, *298*, 2176–2179.

[2] Ye, X. C.; Collins, J. E.; Kang, Y. J.; Chen, J.; Chen, D. T. N.; Yodh, A. G.; Murray, C. B. Morphologically controlled synthesis of colloidal upconversion nanophosphors and their shape-directed self-assembly. *Proc. Natl. Acad. Sci. USA* **2010**, *107*, 22430–22435.

[3] Lee, I.; Delbecq, F.; Morales, R.; Albiter, M. A.; Zaera, F. Tuning selectivity in catalysis by controlling particle shape. *Nat. Mater.* **2009**, *8*, 132–138.

[4] Lee, K. S.; El-Sayed, M. A. Gold and silver nanoparticles in sensing and imaging: Sensitivity of plasmon response to size, shape, and metal composition. *J. Phys. Chem. B* **2006**, *110*, 19220–19225.

[5] Grzelczak, M.; Pérez-Juste, J.; Mulvaney, P.; Liz-Marzan, L. M. Shape control in gold nanoparticle synthesis. *Chem. Soc. Rev.* **2008**, *37*, 1783–1791.

[6] Murphy, C. J.; Sau, T. K.; Gole, A. M.; Orendorff, C. J.; Gao, J. X.; Gou, L. F.; Hunyadi, S. E.; Li, T. Anisotropic metal nanoparticles: Synthesis, assembly, and optical applications. *J. Phys. Chem. B* **2005**, *109*, 13857–13870.

[7] Wang, Y. L.; Xia, Y. N. Bottom-up and top-down approaches to the synthesis of monodispersed spherical colloids of low melting-point metals. *Nano Lett.* **2004**, *4*, 2047–2050.

[8] Merkel, T. J.; Herlihy, K. P.; Nunes, J.; Orgel, R. M.; Rolland, J. P.; DeSimone, J. M. Scalable, shape-specific, top-down fabrication methods for the synthesis of engineered colloidal particles. *Langmuir* **2010**, *26*, 13086–13096.

[9] Sau, T. K.; Rogach, A. L. *Complex-Shaped Metal Nanoparticles*: *Bottom-Up Syntheses and Applications*; Wiley-VCH: Weinheim, 2012.

[10] Langille, M. R.; Personick, M. L.; Zhang, J.; Mirkin, C. A. Bottom-up synthesis of gold octahedra with tailorable hollow features. *J. Am. Chem. Soc.* **2011**, *133*, 10414–10417.

[11] Chung, S. W.; Ginger, D. S.; Morales, M. W.; Zhang, Z. F.; Chandrasekhar, V.; Ratner, M. A.; Mirkin, C. A. Top-down meets bottom-up: Dip-pen nanolithography and DNA-directed assembly of nanoscale electrical circuits. *Small* **2005**, *1*, 64–69.

[12] Kazem, N.; Hellebrekers, T.; Majidi, C. Soft multifunctional composites and emulsions with liquid metals. *Adv. Mater.* **2017**, *29*, 1605985.

[13] Dickey, M. D. Stretchable and soft electronics using liquid metals. *Adv. Mater.* **2017**, *29*, 1606425.

[14] Wang, Q.; Yu, Y.; Liu, J. Preparations, characteristics and applications of the functional liquid metal materials. *Adv. Eng. Mater.* **2018**, *20*, 1700781.

[15] Yan, J. J.; Lu, Y.; Chen, G. J.; Yang, M.; Gu, Z. Advances in liquid metals for biomedical applications. *Chem. Soc. Rev.* **2018**, *47*, 2518–2533.

[16] Taccardi, N.; Grabau, M.; Debuschewitz, J.; Distaso, M.; Brandl, M.; Hock, R.; Maier, F.; Papp, C.; Erhard, J.; Neiss, C. et al. Gallium-rich Pd-Ga phases as supported liquid metal catalysts. *Nat. Chem.* **2017**, *9*, 862–867.

[17] Lu, Y.; Hu, Q. Y.; Lin, Y. L.; Pacardo, D. B.; Wang, C.; Sun, W. J.; Ligler, F. S.; Dickey, M. D.; Gu, Z. Transformable liquid-metal nanomedicine. *Nat. Commun.* **2015**, *6*, 10066.

[18] Hohman, J. N.; Kim, M.; Wadsworth, G. A.; Bednar, H. R.; Jiang, J.; LeThai, M. A.; Weiss, P. S. Directing substrate morphology via self-assembly: Ligand-mediated scission of gallium-indium microspheres to the nanoscale. *Nano Lett.* **2011**, *11*, 5104–5110.

[19] Chechetka, S. A.; Yu, Y.; Zhen, X.; Pramanik, M.; Pu, K. Y.; Miyako, E. Light-driven liquid metal nanotransformers for biomedical theranostics. *Nat. Commun.* **2017**, *8*, 15432.

[20] Yamaguchi, A.; Mashima, Y.; Iyoda, T. Reversible size control of liquid-metal nanoparticles under ultrasonication. *Angew. Chem., Int. Ed.* **2015**, *54*, 12809–12813.

[21] Ren, L.; Zhuang, J. C.; Casillas, G.; Feng, H. F.; Liu, Y. Q.; Xu, X.; Liu, Y. D.; Chen, J.; Du, Y.; Jiang, L. et al. Nanodroplets for stretchable superconducting circuits. *Adv. Funct. Mater.* **2016**, *26*, 8111–8118.

[22] Lu, Y.; Lin, Y. L.; Chen, Z. W.; Hu, Q. Y.; Liu, Y.; Yu, S. J.; Gao, W.; Dickey, M. D.; Gu, Z. Enhanced endosomal escape by light-fueled liquid-metal transformer. *Nano Lett.* **2017**, *17*, 2138–2145.

[23] Lin, Y. L.; Liu, Y.; Genzer, J.; Dickey, M. D. Shape-transformable liquid metal nanoparticles in aqueous solution. *Chem. Sci.* **2017**, *8*, 3832–3837.

[24] Negishi, Y.; Nobusada, K.; Tsukuda, T. Glutathione-protected gold clusters revisited: Bridging the gap between gold(I)−thiolate complexes and thiolate-protected gold nanocrystals. *J. Am. Chem. Soc.* **2005**, *127*, 5261–5270.

[25] Sun, W. J.; Hu, Q. Y.; Ji, W. Y.; Wright, G.; Gu, Z. Leveraging physiology for precision drug delivery. *Physiol. Rev.* **2017**, *97*, 189–225.

[26] Miljevic, B.; Hedayat, F.; Stevanovic, S.; Fairfull-Smith, K. E.; Bottle, S. E.; Ristovski, Z. D. To sonicate or not to sonicate pm filters: Reactive oxygen species generation upon ultrasonic irradiation. *Aerosol Sci. Technol.* **2014**, *48*, 1276–1284.

[27] Liu, Y. L.; Ai, K. L.; Lu, L. H. Polydopamine and its derivative materials: Synthesis and promising applications in energy, environmental, and biomedical fields. *Chem. Rev.* **2014**, *114*, 5057–5115.

[28] Li, S. C.; Chu, L. N.; Gong, X. Q.; Diebold, U. Hydrogen bonding controls the dynamics of catechol adsorbed on a TiO_2(110) surface. *Science* **2010**, *328*, 882–884.

[29] Fan, Q. L.; Cheng, K.; Hu, X.; Ma, X. W.; Zhang, R. P.; Yang, M.; Lu, X. M.; Xing, L.; Huang, W.; Gambhir, S. S. et al. Transferring biomarker into molecular probe: Melanin nanoparticle as a naturally active platform for multimodality imaging. *J. Am. Chem. Soc.* **2014**, *136*, 15185–15194.

[30] Huang, X. H.; El-Sayed, I. H.; Qian, W.; El-Sayed, M. A. Cancer cell imaging and photothermal therapy in the near-infrared region by using gold nanorods. *J. Am. Chem. Soc.* **2006**, *128*, 2115–2120.

[31] Lal, S.; Clare, S. E.; Halas, N. J. Nanoshell-enabled photothermal cancer therapy: Impending clinical impact. *Acc. Chem. Res.* **2008**, *41*, 1842–1851.

[32] Lyu, Y.; Fang, Y.; Miao, Q. Q.; Zhen, X.; Ding, D.; Pu, K. Y. Intraparticle molecular orbital engineering of semiconducting polymer nanoparticles as amplified theranostics for *in vivo* photoacoustic imaging and photothermal therapy. *ACS Nano* **2016**, *10*, 4472–4481.

[33] Lovell, J. F.; Jin, C. S.; Huynh, E.; Jin, H. L.; Kim, C.; Rubinstein, J. L.; Chan, W. C. W.; Cao, W. G.; Wang, L. V.; Zheng, G. Porphysome nanovesicles generated by porphyrin bilayers for use as multimodal biophotonic contrast agents. *Nat. Mater.* **2011**, *10*, 324–332.

[34] Zhang, Y. M.; Hong, H.; Sun, B. Y.; Carter, K.; Qin, Y. R.; Wei, W.; Wang, D. P.; Jeon, M.; Geng, J. M.; Nickles, R. J. et al. Surfactant-stripped naphthalocyanines for multimodal tumor theranostics with upconversion guidance cream. *Nanoscale* **2017**, *9*, 3391–3398.

[35] Mackey, M. A.; Ali, M. R. K.; Austin, L. A.; Near, R. D.; El-Sayed, M. A. The most effective gold nanorod size for plasmonic photothermal therapy: Theory and *in vitro* experiments. *J. Phys. Chem. B* **2014**, *118*, 1319–1326.

[36] Yang, M.; Fan, Q. L.; Zhang, R. P.; Cheng, K.; Yan, J. J.; Pan, D. H.; Ma, X. W.; Lu, A.; Cheng, Z. Dragon fruit-like biocage as an iron trapping nanoplatform for high efficiency targeted cancer multimodality imaging. *Biomaterials* **2015**, *69*, 30–37.

[37] Yan, J. J.; Ji, Y.; Zhang, P. J.; Lu, X. M.; Fan, Q. L.; Pan, D. H.; Yang, R. L.; Xu, Y. P.; Wang, L. Z.; Zhang, L. et al. Melanin nanoparticles as an endogenous agent for efficient iron overload therapy. *J. Mater. Chem. B* **2016**, *4*, 7233–7240.

[38] Hudson, Z. M.; Boott, C. E.; Robinson, M. E.; Rupar, P. A.; Winnik, M. A.; Manners, I. Tailored hierarchical micelle architectures using living crystallization-driven self-assembly in two dimensions. *Nat. Chem.* **2014**,

6, 893–898.
[39] Wang, J.; Zhu, W.; Peng, B.; Chen, Y. M. A facile way to prepare crystalline platelets of block copolymers by crystallization-driven self-assembly. *Polymer* **2013**, *54*, 6760–6767.
[40] Zhou, Y.; Yan, B.; He, X. H. Controlled synthesis and up/down-conversion luminescence of self-assembled hierarchical architectures of monoclinic $AgRE(WO_4)_2$: Ln^{3+} (RE = Y, La, Gd, Lu; Ln = Eu, Tb, Sm, Dy, Yb/Er, Yb/Tm). *J. Mater. Chem. C* **2014**, *2*, 848–855.
[41] Rebolledo, A. F.; Bomatí-Miguel, O.; Marco, J. F.; Tartaj, P. A facile synthetic route for the preparation of superparamagnetic iron oxide nanorods and nanorices with tunable surface functionality. *Adv. Mater.* **2008**, *20*, 1760–1765.
[42] Wang, H.; Brandl, D. W.; Le, F.; Nordlander, P.; Halas, N. J. Nanorice: A hybrid plasmonic nanostructure. *Nano Lett.* **2006**, *6*, 827–832.
[43] Parasuraman, P. S.; Tsai, H. C.; Imae, T. *In-situ* hydrothermal synthesis of carbon nanorice using nafion as a template. *Carbon* **2014**, *77*, 660–666.
[44] Hoshyargar, F.; Crawford, J.; O'Mullane, A. P. Galvanic replacement of the liquid metal Galinstan. *J. Am. Chem. Soc.* **2017**, *139*, 1464–1471.
[45] Glass, K.; Ito, S.; Wilby, P. R.; Sota, T.; Nakamura, A.; Bowers, C. R.; Vinther, J.; Dutta, S.; Summons, R.; Briggs, D. E. G. et al. Direct chemical evidence for Eumelanin pigment from the Jurassic period. *Proc. Natl. Acad. Sci. USA* **2012**, *109*, 10218–10223.
[46] Mbonyiryivuze, A.; Mwakikunga, B.; Dhlamini, S. M.; Maaza, M. Fourier transform infrared spectroscopy for sepia melanin. *Phys. Mater. Chem.* **2015**, *3*, 25–29.
[47] Zangmeister, R. A.; Morris, T. A.; Tarlov, M. J. Characterization of polydopamine thin films deposited at short times by autoxidation of dopamine. *Langmuir* **2013**, *29*, 8619–8628.
[48] Tas, A. C.; Majewski, P. J.; Aldinger, F. Synthesis of gallium oxide hydroxide crystals in aqueous solutions with or without urea and their calcination behavior. *J. Am. Ceram. Soc.* **2002**, *85*, 1421–1429.
[49] Bronze-Uhle, E. S.; Paulin, J. V.; Piacenti-Silva, M.; Battocchio, C.; Rocco, M. L. M.; de Oliveira Graeff, C. F. Melanin synthesis under oxygen pressure. *Polym. Int.* **2016**, *65*, 1339–1346.
[50] Rajh, T.; Chen, L. X.; Lukas, K.; Liu, T.; Thurnauer, M. C.; Tiede, D. M. Surface restructuring of nanoparticles: An efficient route for ligand-metal oxide crosstalk. *J. Phys. Chem. B* **2002**, *106*, 10543–10552.
[51] Huang, C. C.; Yeh, C. S.; Ho, C. J. Laser ablation synthesis of spindle-like gallium oxide hydroxide nanoparticles with the presence of cationic cetyltrimethylammonium bromide. *J. Phys. Chem. B* **2004**, *108*, 4940–4945.
[52] Rao, W.; Liu, J. Injectable liquid alkali alloy based-tumor thermal ablation therapy. *Minim. Invasive Ther. Allied Technol.* **2009**, *18*, 30–35.
[53] Yang, X.; Yang, M. X.; Pang, B.; Vara, M.; Xia, Y. N. Gold nanomaterials at work in biomedicine. *Chem. Rev.* **2015**, *115*, 10410–10488.
[54] Ye, Y. Q.; Wang, C.; Zhang, X. D.; Hu, Q. Y.; Zhang, Y. Q.; Liu, Q.; Wen, D.; Milligan, J.; Bellotti, A.; Huang, L. et al. A melanin-mediated cancer immunotherapy patch. *Sci. Immunol.* **2017**, *2*, eaan5692.
[55] Zhang, L.; Sheng, D. L.; Wang, D.; Yao, Y. Z.; Yang, K.; Wang, Z. G.; Deng, L. M.; Chen, Y. Bioinspired multifunctional melanin-based nanoliposome for photoacoustic/magnetic resonance imaging-guided efficient photothermal ablation of cancer. *Theranostics* **2018**, *8*, 1591–1606.
[56] Shao, J. D.; Xie, H. H.; Huang, H.; Li, Z. B.; Sun, Z. B.; Xu, Y. H.; Xiao, Q. L.; Yu, X. F.; Zhao, Y. T.; Zhang, H. et al. Biodegradable black phosphorus-based nanospheres for *in vivo* photothermal cancer therapy. *Nat. Commun.* **2016**, *7*, 12967.
[57] Huang, H. C.; Rege, K.; Heys, J. J. Spatiotemporal temperature distribution and cancer cell death in response to extracellular hyperthermia induced by gold nanorods. *ACS Nano* **2010**, *4*, 2892–2900.
[58] Cheng, L.; Wang, C.; Feng, L. Z.; Yang, K.; Liu, Z. Functional nanomaterials for phototherapies of cancer. *Chem. Rev.* **2014**, *114*, 10869–10939.
[59] Ahmed, M.; Brace, C. L.; Lee, F. T.; Goldberg, S. N. Principles of and advances in percutaneous ablation. *Radiology* **2011**, *258*, 351–369.
[60] Yu, J. C.; Zhang, Y. Q.; Ye, Y. Q.; DiSanto, R.; Sun, W. J.; Ranson, D.; Ligler, F. S.; Buse, J. B.; Gu, Z. Microneedle-array patches loaded with hypoxia-sensitive vesicles provide fast glucose-responsive insulin delivery. *Proc. Natl. Acad. Sci. USA* **2015**, *112*, 8260–8265.
[61] Willcock, H.; Lu, A.; Hansell, C. F.; Chapman, E.; Collins, I. R.; O'Reilly, R. K. One-pot synthesis of responsive sulfobetaine nanoparticles by RAFT polymerisation: The effect of branching on the UCST cloud point. *Polym. Chem.* **2014**, *5*, 1023–1030.